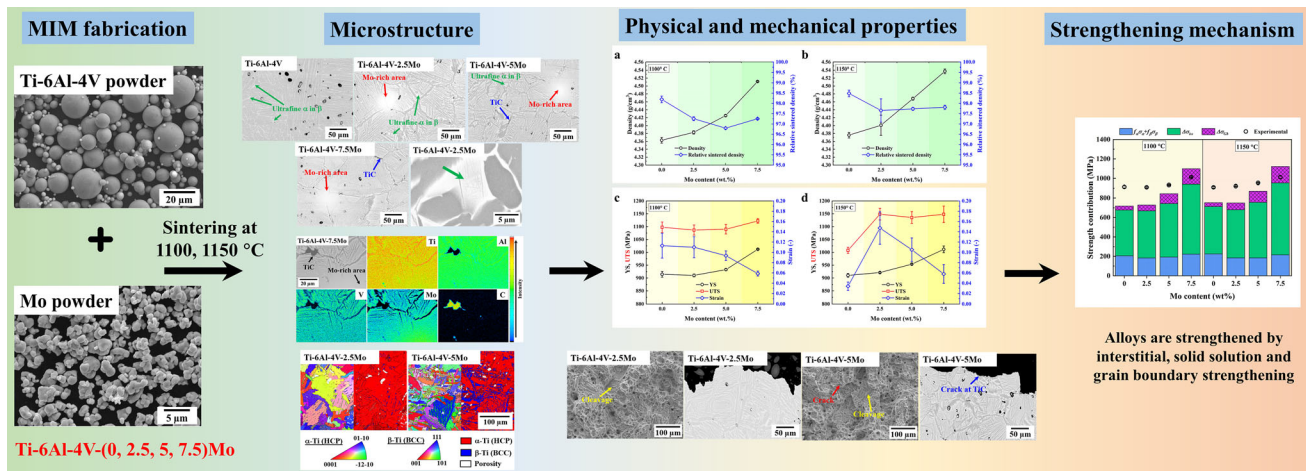


Microstructures and Tensile Properties of Ti-6Al-4 V-(0, 2.5, 5, 7.5)Mo Alloys Manufactured by Metal Injection Molding



CHANUN SUWANPREECHA, SUKRIT SONGKUEA, MAKIKO TANGE, and ANCHALEE MANONUKUL

Ti-6Al-4 V is the most widely utilized titanium alloy. Mo is a β -stabilizing element, which can modify the microstructure and tensile properties of titanium alloys. In this work, the effects of Mo additions to Ti-6Al-4 V manufactured by metal injection molding were investigated. Sintering temperatures of 1100 and 1150 °C were employed to examine the microstructures and tensile properties. The tensile properties varied with Mo content and sintering temperature. Specifically, the ultimate tensile strength increased with Mo content at both temperatures. The strain to failure tended to decrease with Mo content when sintered at 1100 °C. However, at 1150 °C, the strain to failure significantly increased with a 2.5 wt pct Mo addition but decreased with the higher Mo additions. The strain to failure improved with a higher volume fraction of grain boundary α layers induced by Mo additions. However, at high Mo contents (> 5 wt pct Mo), the fracture was primarily governed by TiC. Hence, 5 wt pct of Mo addition is considered the threshold. In this study, Ti-6Al-4 V-2.5Mo sintered at 1150 °C exhibited the most optimal properties, making it an attractive choice for functional materials.



<https://doi.org/10.1007/s11661-023-07292-6>

© The Minerals, Metals & Materials Society and ASM International 2024

I. INTRODUCTION

TITANIUM (Ti) and its alloys have been widely employed in many industries, *e.g.*, automotive, aerospace, marine, and biomedical applications because of its high strength-to-weight ratio, good corrosion resistance, and excellent biocompatibility.^[1] However, the fabrication of Ti and its alloys poses challenges due to their reactivity with oxygen.^[2] Conventional manufacturing processes, *e.g.*, machining, forging, and casting, become less cost competitive when dealing with highly complex parts and generate significant waste swarf.

CHANUN SUWANPREECHA, SUKRIT SONGKUEA, and ANCHALEE MANONUKUL are with the National Metal and Materials Technology Center (MTEC), National Sciences and Technology Development Agency (NSTDA), 111 Thailand Science Park, Paholyothin Rd., Klong Nung, Klong Luang, Pathumthani 12120, Thailand. Contact e-mail: anchalm@mtec.or.th MAKIKO TANGE is with the Taisei Kogyo (Thailand) Co., Ltd., Room INC2D-409, Innovation Cluster 2 Building, Tower D, 141 Thailand Science Park, Paholyothin Rd., Klong Nung, Klong Luang, Pathumthani 12120, Thailand.

Manuscript submitted August 9, 2023; accepted December 20, 2023.

Article published online January 20, 2024

Metal injection molding (MIM) is an alternative mass-production process for Ti alloys. MIM enables the fabrication of near-net-shape parts with intricate geometries, precise dimensional control, and high accuracy.^[3–6] MIM has proven to be a successful method for manufacturing different types of titanium alloys, such as α ,^[7,8] $\alpha + \beta$,^[9–13] β ,^[14–17] and γ -typed^[18,19] alloys. These alloys demonstrate exceptional mechanical properties and high density.^[6,10–12,18]

In high-performance structural applications, titanium alloys that consist of α and β structures are typically suitable.^[1] The most utilized alloy in this category is Ti-6Al-4 V, which accounts for 50 pct of total titanium alloy usage. This alloy is preferred due to its excellent overall mechanical properties, performance, and enhanced workability.^[1,20] The strength and ductility of $\alpha + \beta$ -typed Ti alloys are primarily influenced by the phase fractions, microstructure, and chemical compositions of the α and β phases. These mechanical properties are normally dominated by their phase fractions, microstructure, and chemical compositions of the α and β phases, which can be tailored by controlling the alloying elements, their concentrations, and employing specific heat treatment processes.^[1,21]

To enhance the mechanical properties of Ti-6Al-4 V alloys, studies have been conducted on the addition of β -phase stabilizers, *e.g.*, Fe,^[22–24] Cr,^[23,25,26] and Mo.^[27–30] The 2 wt pct Fe addition in Ti-6Al-4 V, fabricated by thermomechanical powder consolidation, results in the refinement of α/β lamellar structures or the transformation of lamellar structure into the ultrafine β structure, leading to a substantial improvement in the strength of Ti-6Al-4 V alloys.^[22] However, excessive Fe content decreases ductility due to pronounced strain localization at the grain boundaries of the α layers.^[22] Similar content of Fe is suggested to improve the mechanical properties of MIM Ti-6Al-4 V.^[23] In the case of Cr additions in Ti-6Al-4 V, it produces a similar strengthening effect to Fe, with strength increasing as the Fe or Cr content rises, but not surpassing a certain threshold.^[25] Achieving a desirable balance between strength and ductility enhancement in the MIM process is accomplished with a 4 wt pct Cr addition.^[23]

Mo is an effective isomorphous β -stabilizing alloying element, which provides both stabilization of the β phase and solid-solution strengthening in Ti alloys. The Mo addition in Ti alloys has been used to develop new functional materials, *e.g.*, biomedical and aerospace alloys.^[31,32] The Mo addition not only simultaneously improves strength and reduces stiffness,^[13] but also enhances corrosion resistance,^[13,33–35] which is favorable for biomedical implants. In addition, Mo can enhance mechanical properties at elevated temperatures^[1] and tribological properties,^[29] which are beneficial to aerospace and high-performance applications. Although the effects of Mo addition in Ti alloys on mechanical properties and microstructure have been previously reported, the effect of Mo addition in Ti-6Al-4 V remains limited compared to Cr and Fe, as mentioned above. Ti-6Al-4 V alloy with 5 wt pct Mo addition fabricated by the conventional powder metallurgy process exhibits superior hardness and wear properties.

Nonetheless, excessive Mo content results in lower mechanical properties.^[29] Similarly, for spark plasma sintering process, 2–4 wt pct Mo additions in Ti-6Al-4 V demonstrate the best balance between strength and ductility.^[30] However, when the Mo content exceeds 4 wt pct, the strength decreases. Undissolved Mo particles can be observed in all Mo-containing specimens.^[30] To the best of our knowledge, there is only one study on the addition of Mo to Ti-6Al-4 V alloy fabricated by MIM.^[28] It reports that an increase in Mo content (1–5 wt pct) results in increasing strength and slightly decreasing in ductility.^[28] A 4 wt pct Mo addition in Ti-6Al-4 V alloy is suggested to provide a balanced combination between strength and ductility because of the formation of a fine structure. No TiC is found within the 1–5 wt pct additions of Mo.^[28] This suggests that in this particular study,^[28] the Mo addition has not reached the critical threshold. However, in other Ti alloys with high concentrations of β -phase stabilizers, TiC usually forms.^[13,17,36] The excessive addition of β -phase stabilizers can potentially generate the hard and brittle TiC,^[36,37] where C is unavoidably contaminated from MIM binders and atmosphere during debinding and sintering processes. In addition, these β -phase stabilizer additions noticeably reduce the solubility limit of C in the alloys.^[37,38] The formation of TiC adversely affects the ductility of the alloys.^[14,17,37,39]

Therefore, this study aims to identify the threshold for Mo addition in Ti-6Al-4 V alloy fabricated by MIM and examine the effect of elemental Mo powder additions (2.5, 5, and 7.5 wt pct) on density, microstructure, and mechanical properties. Two sintering temperatures (1100 and 1150 °C) for 4 h are employed. Furthermore, the relationships between microstructure, impurities, and their mechanical properties are investigated. The microstructure, TiC, and impurities are analyzed by scanning electron microscopy (SEM) equipped with electron backscatter diffraction (EBSD), electron probe microanalyzer (EPMA), and X-ray diffraction (XRD). Tensile testing and Vickers microhardness are utilized to assess mechanical properties. To understand the failure mechanism, the fracture surface and cross section of the fractured specimens are investigated.

II. EXPERIMENTAL PROCEDURES

A. Preparation of Specimens

Figure 1 shows gas-atomized pre-alloyed Ti-6Al-4 V and elemental Mo powders with the mean particle sizes (D_{50}) of 12 and 5.5 μm , respectively, used for MIM fabrication. The chemical compositions and impurity supplied by the suppliers and reported in Table I, exhibit low initial impurity content. The metallic powders with 65 vol. pct solid loading were mixed with a polyacetal-based binder supplied by Taisei Kogyo Co., Ltd., Japan to form a batch of feedstock with the compositions of 0, 2.5, 5, and 7.5 pct Mo (from here, all pct will be in wt pct if not stated). Each feedstock was then crushed, sieved, and injected using a Niigata (MD50s-IV) injection molding machine to create the

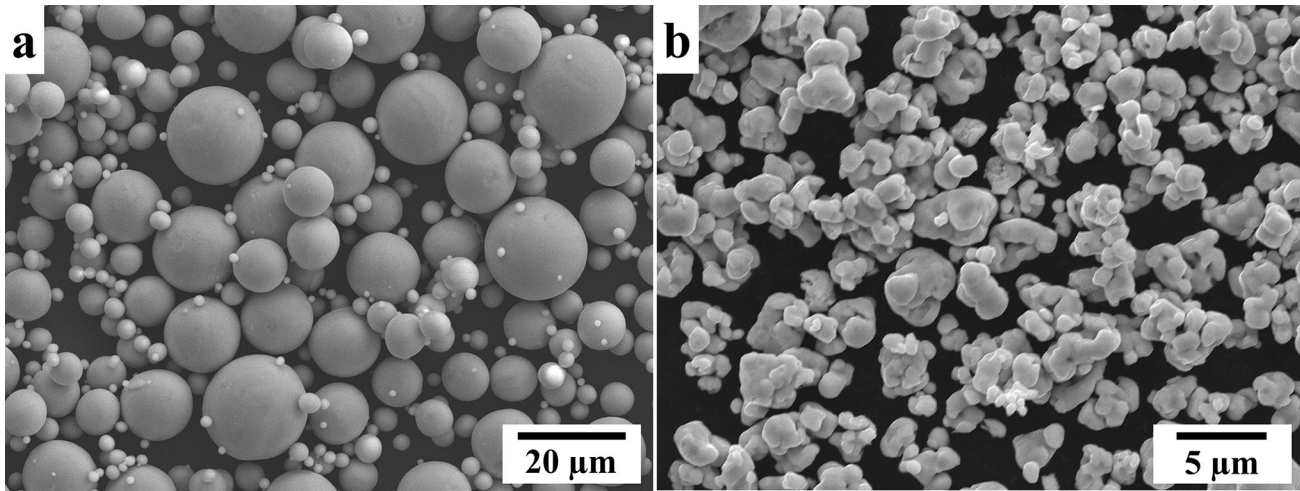


Fig. 1—Micrographs of; (a) gas-atomized spherical Ti-6Al-4V powder and (b) elemental rounded Mo powder with some agglomeration.

Table I. Mean Powder Size and Chemical Composition of as-Received Powders Used

Powder	D_{50} (μm)	Element (Wt Pct)								
		Al	V	Mo	C	O	N	H	Fe	Ti
Ti-6Al-4 V Gr5	12	6.48	4.1	—	0.02	0.19	0.02	0.003	0.21	Bal.
Mo	5.5	—	—	> 99.9	—	0.07	—	—	0.003	—

green tensile specimens with a width of 6 mm at gage length and a thickness of 3.5 mm, following ASTM E8/E8M – 21. The green parts were debound at 500 °C for 1 h in an Ar-flow atmosphere (the debinding condition was in-house optimized through weight loss analysis to ensure the complete removal of all binders) before continuously being sintered in a vacuum atmosphere ($>10^{-4}$ Pa) using a Shimadzu (VHLgr20/20/23) sintering furnace in one single thermal cycle. The sintering conditions were 1100 and 1150 °C for 4 h. Table II lists the parameters used for MIM fabrications.

B. Microstructural and Mechanical Examinations

The as-sintered density was determined using the Archimedes' principle. Eq. [1] is used to calculate the relative as-sintered density.

$$\text{Relative as - sintered density(pct)} = \frac{\rho}{\rho_0} \times 100, \quad [1]$$

where ρ is the measured as-sintered density. In addition, ρ_0 is the theoretical density of Ti-6Al-4 V-xMo alloys calculated using the rule of mixture as shown in Eq. [2].

$$\rho_0 = 1 / \left(\frac{X_{\text{Ti}}}{\rho_{\text{Ti}}} + \frac{X_{\text{Mo}}}{\rho_{\text{Mo}}} \right), \quad [2]$$

Table II. MIM Process Parameters

Parameters	Values
Powder:Binder Ratio	65:35 (vol pct)
Ti-6Al-4 V Powder Density	4.443 g/cm ³
Pure Mo Powder Density	10.16 g/cm ³
Blended Polymer Binder Density	0.9621 g/cm ³
Injection Temperature	165 °C
Mold Temperature	40 °C
Debinding Temperature and Time	500 °C for 2 h
Sintering Temperature and Time	1100 and 1150 °C for 4 h

where X_{Ti} and X_{Mo} are the mass fractions of Ti-6Al-4 V and Mo, respectively; ρ_{Ti} and ρ_{Mo} are the densities of the Ti-6Al-4 V and Mo powders, respectively, as listed in Table II.

A standard metallographic method was used to prepare the sintered specimens for microstructural analysis. Microstructures were observed using a JEOL (JSM 7800F FE-SEM) scanning electron microscope (SEM) equipped with energy-dispersive X-ray spectroscopy (EDS) apparatus. The TiC and Mo-rich area were analyzed using a Shimadzu (8050G) EPMA. Phase identification and phase fraction were analyzed using a Rigaku (TTRAX III) X-ray diffractometer with Cu-K α radiation with a 0.02° step size and a 3°/min scanning rate. Electron backscatter diffraction (EBSD) analysis

was carried out using a Hitachi (SU8230) SEM equipped with an EBSD detector. EBSD samples were prepared using a standard metallographic method and subsequently ion milled four times for 5 min each. The impurity (C, H, N, and O) in the sintered specimens was measured using LECO (TC-300 and CS-200) inert gas fusion and combustion machines. Eq. [3]^[6] is used to calculate the O equivalent (O_{eq}) from O, N, and C contents to combine the effects.

$$O_{eq} = O + 2N + 0.75C \text{ (in wt pct)}. \quad [3]$$

Sintered specimens were polished following standard metallographic techniques for Vickers microhardness tests. At least three indents were made for each specimen using a Shimadzu (HMV-G) microhardness tester with 9.807 N load for 15 s. Tensile tests for the as-sintered specimens were carried out at a constant speed of 1 mm/min using an Instron (8872) universal testing machine with a laser extensometer. At least three tensile tests were performed and averaged for the yield strength (YS), ultimate tensile strength (UTS), and strain at break for each condition. Error bars are standard deviations. Furthermore, the cross-sectioned fracture surfaces after tensile testing were investigated by SEM to gain insight into the failure behavior.

III. RESULTS

A. Physical and Microstructure Characterizations

The nominal and experimental compositions of all alloys analyzed by EDS are listed in Table III. Both experimental and nominal compositions are close.

Figure 2 shows (a) the apparent and (b) relative sintered densities of all alloys sintered at 1100 and 1150 °C. As the Mo contents increase, the apparent densities also increase because Mo has higher density

than Ti-6Al-4V. However, the Mo additions result in a slight decrease in relative density, ranging from 98.25 and 98.5 to a constant value of approximately 97 and > 97.5 pct at the sintering temperatures of 1100 and 1150 °C, respectively. These decreases are attributed to the lower diffusivity of Mo in Ti than the self-diffusion of Ti.^[40] Consequently, a sintering temperature should be increased for a higher relative sintered density. This observation is consistent with the current findings [Figures 2(a) and (b)], where the 1150 °C sintering temperature demonstrates a higher relative sintered density than 1100 °C across all compositions.

The impurity content and O_{eq} for samples sintered at 1100 and 1150 °C are illustrated in Figure 3. After sintering, H and N contents show negligible increases for both sintering temperatures. However, C and O contents significantly increase relative to their initial values as powder (Table I). This can be attributed to the uptake of C from the binder and C and O from the atmosphere, which is never entirely free from impurities during the debinding and sintering processes.^[7] In general, higher sintering temperatures lead to more reactivity and picking up of O, as observed in Mo-free alloys. However, Mo-containing alloys sintered at 1100 °C have slightly higher O contents than 1150 °C. This variation is due to discrepancies in the impurity content arising from different batches of feedstock preparations, despite the application of similar processing parameters. Similar variations have been reported in other studies.^[13,15] The O_{eq} , which combines the effects of O, C, and N, as calculated using Eq. [3], exhibits similar trends of O [Figures 3(a) and (b)]. This indicates that O_{eq} is primarily influenced by the O content in all alloys at both sintering temperatures. From the literature,^[41,42] maintaining O_{eq} below 0.35 wt pct is essential to prevent brittleness in Ti alloys. However, in this study, all conditions exhibit higher O_{eq} content than this limit, which may adversely affect the ductility of the alloy. The slightly elevated O content is attributed to the

Table III. Chemical Compositions of Sintered Specimens from EDS Analysis

Sintering Temperature (°C)	Nominal Composition	Element, Wt Pct (At. Pct)			
		Al	V	Mo	Ti
1100	Ti-6Al-4V	6.2 ± 0.19 (10.51)	2.8 ± 0.10 (2.51)	—	bal.
	Ti-6Al-4V-2.5Mo	6.1 ± 0.01 (10.47)	3.0 ± 0.05 (2.73)	2.4 ± 0.05 (1.16)	bal.
	Ti-6Al-4V-5Mo	5.8 ± 0.02 (10.10)	2.7 ± 0.08 (2.49)	4.8 ± 0.07 (2.35)	bal.
	Ti-6Al-4V-7.5Mo	5.8 ± 0.20 (10.22)	2.8 ± 0.02 (2.61)	7.2 ± 0.03 (3.57)	bal.
1150	Ti-6Al-4V	6.4 ± 0.05 (10.84)	2.8 ± 0.02 (2.51)	—	bal.
	Ti-6Al-4V-2.5Mo	6.3 ± 0.03 (10.80)	2.9 ± 0.05 (2.63)	2.4 ± 0.12 (1.16)	bal.
	Ti-6Al-4V-5Mo	6.2 ± 0.12 (10.77)	3.0 ± 0.10 (2.76)	5.0 ± 0.09 (2.46)	bal.
	Ti-6Al-4V-7.5Mo	6.0 ± 0.04 (10.55)	2.6 ± 0.04 (2.42)	7.2 ± 0.07 (3.57)	bal.

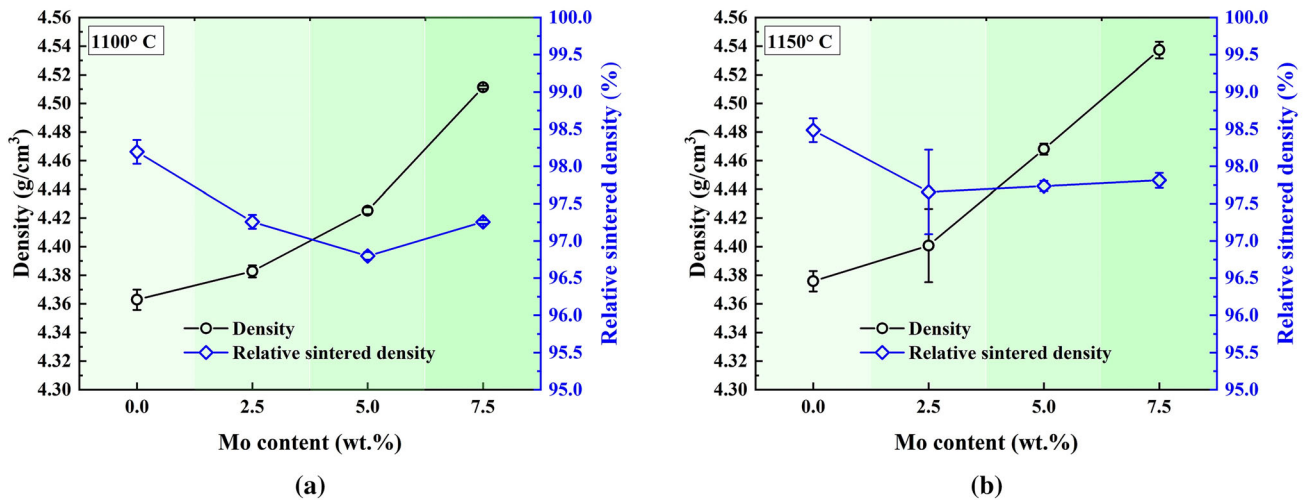


Fig. 2—Apparent and relative as-sintered densities of Ti-6Al-4V-xMo sintered at (a) 1100 °C and (b) 1150 °C for 4 h.

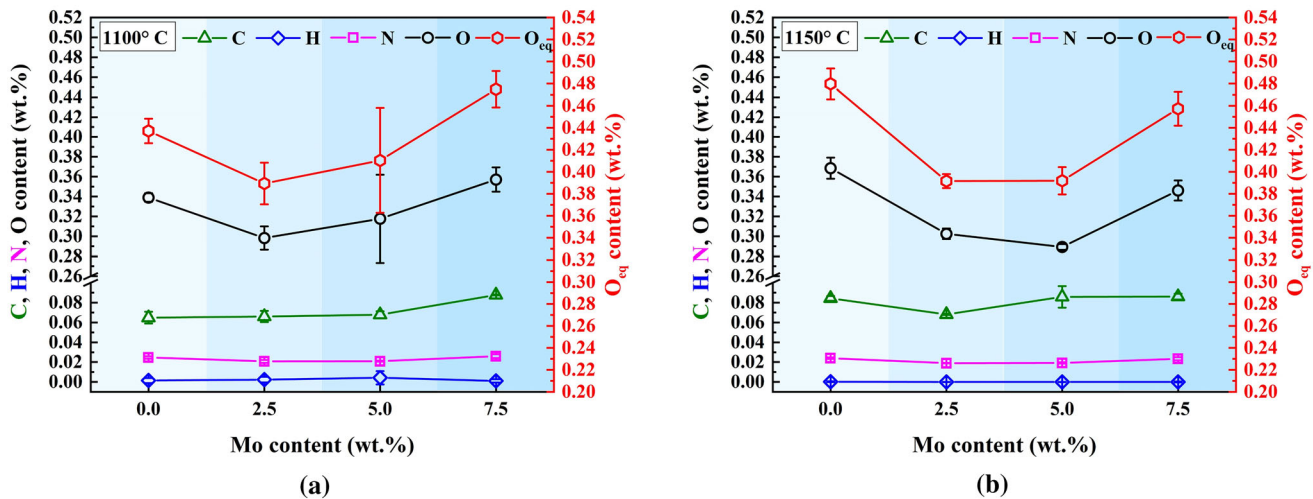


Fig. 3—Impurities content and Oxygen equivalent content (O_{eq}) of samples sintered at (a) 1100 °C and (b) 1150 °C for 4 h.

use of powder with an average size approximately half of a typical Ti-6Al-4 V MIM powder (D_{50} : ~ 20 μm). The effects of interstitial elements on the evolution of mechanical properties will be discussed in more detail.

Figure 4(a) and (b) shows the XRD diffraction patterns of samples sintered at 1100 and (b) 1150 °C, respectively. The results reveal high-intensity α peaks and low-intensity β peaks in Mo-free specimens. The intensity of β peaks rises with the Mo content, while the intensity of α peaks decreases with the displacement of β peaks to lower diffraction angles. The α peaks remain relatively unchanging at both sintering temperatures. Typically, the XRD peaks are displaced to lower angles when the lattice parameters expand due to the addition of solute atoms with larger atomic sizes. However, in this study, Mo has a smaller atomic size compared to Ti. Therefore, the displacement to lower angles is caused by the formation of fine α phases with Mo additions, enhancing the partitioning of Mo and V to form the β phase and enlarging the lattice parameters.^[43] In

addition, the presence of TiC phase is observed in the specimen with a 7.5 wt pct Mo addition for both sintering temperatures.

The XRD results of specimens sintered at both temperatures were used to calculate the phase volume fraction as shown in Figure 5. The α phase fraction decreases with increasing Mo contents, while the β phase fraction increases because of the beta-stabilizing effect of Mo. Up to a 5 wt pct Mo addition, there is a phase fraction difference of less than 10 pct between the two sintering temperatures. However, with a 7.5 wt pct Mo addition, there is an approximate 15 pct difference in the α phase fraction between the sintering temperatures. In addition, the alloy containing 7.5 wt pct Mo sintered at 1150 °C shows a TiC fraction of approximately 4 pct. It is noted that the peak intensity belongs to TiC is lower than XRD detection limit; thus, the volume fraction of TiC cannot be calculated using XRD analysis in some conditions. These results suggest that Mo is not completely dissolved, particularly evident in the Ti-6Al-4 V

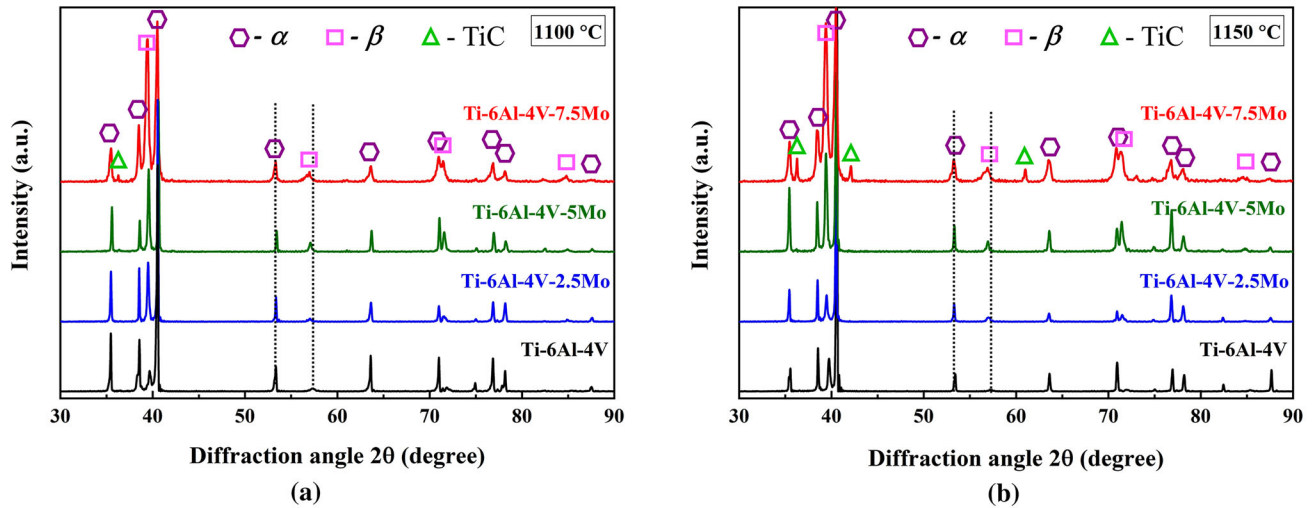


Fig. 4—XRD patterns of Ti-6Al-4V-xMo samples sintered at (a) 1100 and (b) 1150 °C.

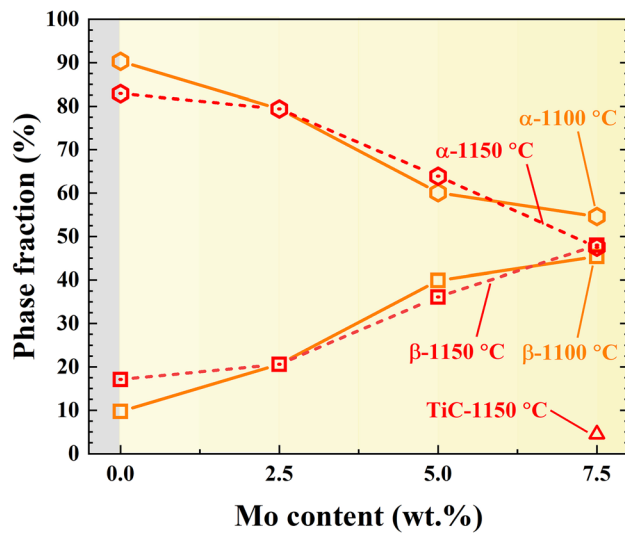


Fig. 5—Phase fractions of Ti-6Al-4V-xMo samples sintered at 1100 and 1150 °C.

alloy containing 7.5 wt pct Mo. The microstructural evidence of undissolved Mo will be presented and discussed next. It is evident that the 1100 °C sintering temperature is insufficient for dissolving 7.5 wt pct Mo; hence, the α phase fraction is higher than anticipated. However, when the alloy is sintered at 1150 °C, a greater amount of Mo is dissolved, leading to a higher β phase fraction that reduces the C solubility limit and consequently generates TiC.

Figure 6 shows the microstructures of Mo-free and Mo-containing Ti-6Al-4 V alloys. In Figure 6(a), the microstructure of Mo-free alloy sintered at 1100 °C exhibits a partly lamella structure with some porosities. However, after sintering at 1150 °C [Figure 6(b)], the microstructure becomes a fully lamella structure with some porosities. For Mo-containing alloys [Figures 6(b) through (d) and (f) through (h)], the α and β lamella

structure inside the grain is finer with increasing Mo contents for both sintering temperatures. Bright spots of Mo-rich areas (undissolved Mo) are also observed in all Mo-containing specimens. When sintering at 1100 °C, Mo-rich areas are barely noticeable in the 2.5 wt pct Mo addition, but more pronounced at higher Mo additions. In addition, fewer Mo-rich areas and a lower concentration of Mo are observed for the same Mo content sintered at 1150 °C. It is noted that Figures 6(b) through (d) and (f) through (h) were specifically taken to show the Mo-rich areas and not to demonstrate their distribution across the specimens. This observation aligns well with the XRD analysis, indicating that the 1100 °C sintering temperature is insufficient to effectively dissolve Mo. At 1150 °C with the same Mo content, a finer α and β lamella structure within the grain is observed. The grain size of samples sintered at 1150 °C is also significantly larger than 1100 °C. Moreover, the presence of ultrafine α within β structure can be observed and identified by the green arrows in Figures 6 and 7, particularly for Mo additions ranging from 0 to 5 wt pct. The formation of this ultrafine α within β structure is associated with the O content and cooling rate,^[43,44] which increase with O content and cooling rate. In the present study, the O contents range from 0.29 to 0.37 wt pct, and the furnace cooling at 10–12 °C /min, which is close to the cooling rate (10 °C /min) in Ti-6Al-4 V-0.49O^[43] and Ti-6Al-7Nb-(0.13-0.48)O^[44] alloys where ultrafine α within β structure was observed.

Furthermore, for both sintering temperatures, the presence of TiC can be observed along the grain boundary as a dark-gray particle in the 5 and 7.5 wt pct Mo additions. The quantity of TiC increases with higher Mo content and becomes detectable by XRD in the alloy sintered at 1150 °C with a 7.5 wt pct Mo addition [Figure 4(b)]. The formation of TiC is confirmed by EPMA analysis as shown in Figure 8, where the dark-gray particle is primarily composed of Ti and C. It is worth noting that a previous study^[28] reported no observation of TiC in MIM Ti-6Al-4 V alloy with 1–5 wt pct Mo addition. This discrepancy could arise

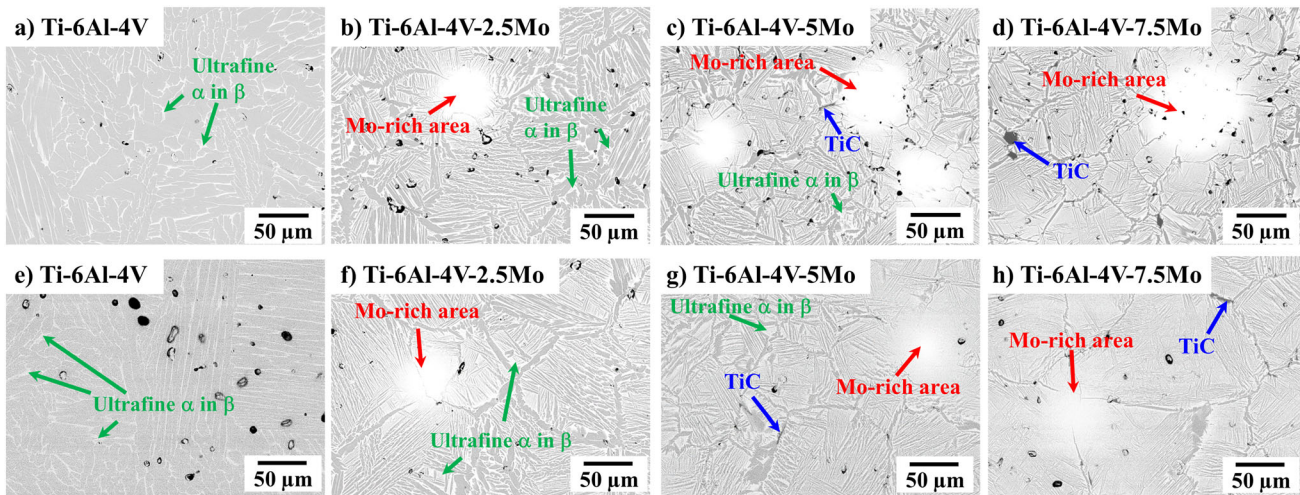


Fig. 6—BSE-SEM micrographs of Ti-6Al-4V-xMo alloys sintered at (a) to (d) 1100 and (e) to (h) 1150 °C for 4 h.

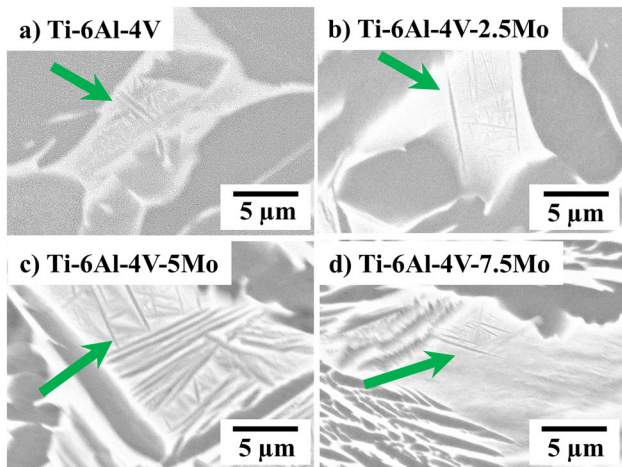


Fig. 7—BSE-SEM micrograph at ultrafine α in β region of Ti-6Al-4V alloys with (a) 0, (b) 2.5, (c) 5 and (d) 7.5 wt pct of Mo sintered at 1150 °C for 4 h.

from various factors, for example, the use of different Ti-6Al-4 V powders and binder, or debinding, and sintering methods.

Figure 9 shows the inverse pole figure and phase maps of Mo-free and Mo-containing alloys. For Mo-free specimens sintered at both sintering temperatures, the crystallographic orientation and phase maps exhibit a high degree of similarity. In Mo-containing alloys, the crystallographic orientation shows a finer microstructure with increasing Mo contents. Furthermore, at the 1100 °C sintering temperature, there is a significant area of β phase corresponding to the Mo-rich area [Figure 9(d)], consistent with the SEM results [Figures 6(c), (d)]. However, when sintered at 1150 °C, Mo can be more dissolved, leading to more α -phase to β -phase transformation [Figure 9(h)]. However, for the Ti-6Al-4 V-7.5Mo alloy sintered at 1150 °C, there is a

lower fraction of large β phase than 1100 °C. This can be explained through the formation of a very fine α and β structure inside the grain [as observed in Figure 6(h)] resulting in the resolution of EBSD analysis (step size) being insufficient to differentiate this fine structure.

B. Mechanical Properties

Figure 10 shows the Vickers microhardness of all specimens is shown. Interestingly, the Mo-free specimens sintered at 1100 °C show significantly higher hardness than 1150 °C. This can be due to the microstructural evolution, transitioning from a partly lamella structure sintered at 1100 °C [Figure 6(a)], to a fully lamella structure sintered at 1150 °C [Figure 6(e)]. For Mo-containing alloys, the hardness increases with higher sintering temperature and Mo content.

The relationship between Mo content, sintering temperature, and the tensile properties of the alloys is shown in Figure 11. At an 1100 °C sintering temperature, the strength of Mo-containing alloys increases with higher Mo content, while the strain to failure decreases until reaching the lowest value with a Mo addition of 7.5 wt pct. At a 1150 °C sintering temperature, the Mo-free specimen exhibits lower strength and strain to failure compared to Mo-containing alloys, which well agrees with the microhardness results, despite having a higher relative sintered density (Figure 2). Among all the alloys studied, the tensile properties of the Ti-6Al-4 V specimens with a 2.5 wt pct Mo addition demonstrate the optimum tensile properties. However, when the Mo content exceeds 2.5 wt pct, the strain to failure decreases even though the tensile strength increases. Considering the effect of sintering temperature, for Mo-free specimens, a 1100 °C sintering temperature results in higher tensile properties than 1150 °C, consistent with the hardness results (Figure 10). On the other hand, for Mo-containing alloys, the higher sintering temperature provides higher or comparable tensile properties in all alloys.

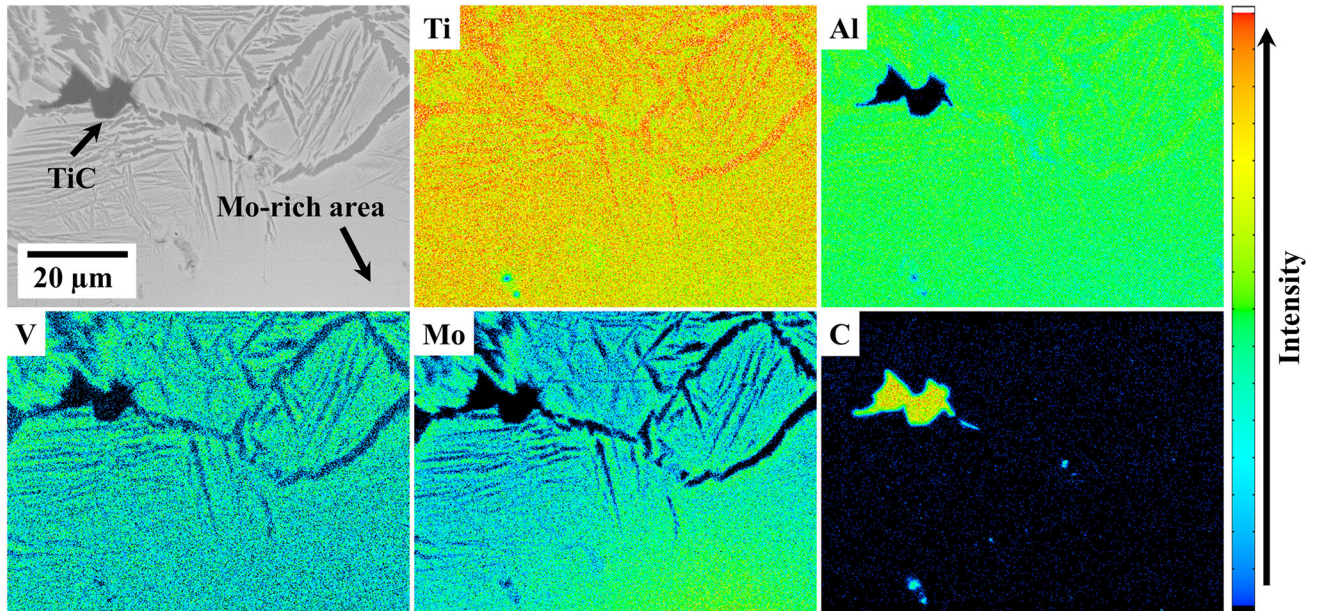


Fig. 8—EPMA result of Ti-6Al-4 V-7.5Mo specimen sintered at 1100 °C for 4 h, showing a Mo-rich area (lower right corner) and a TiC particle at the grain boundary.

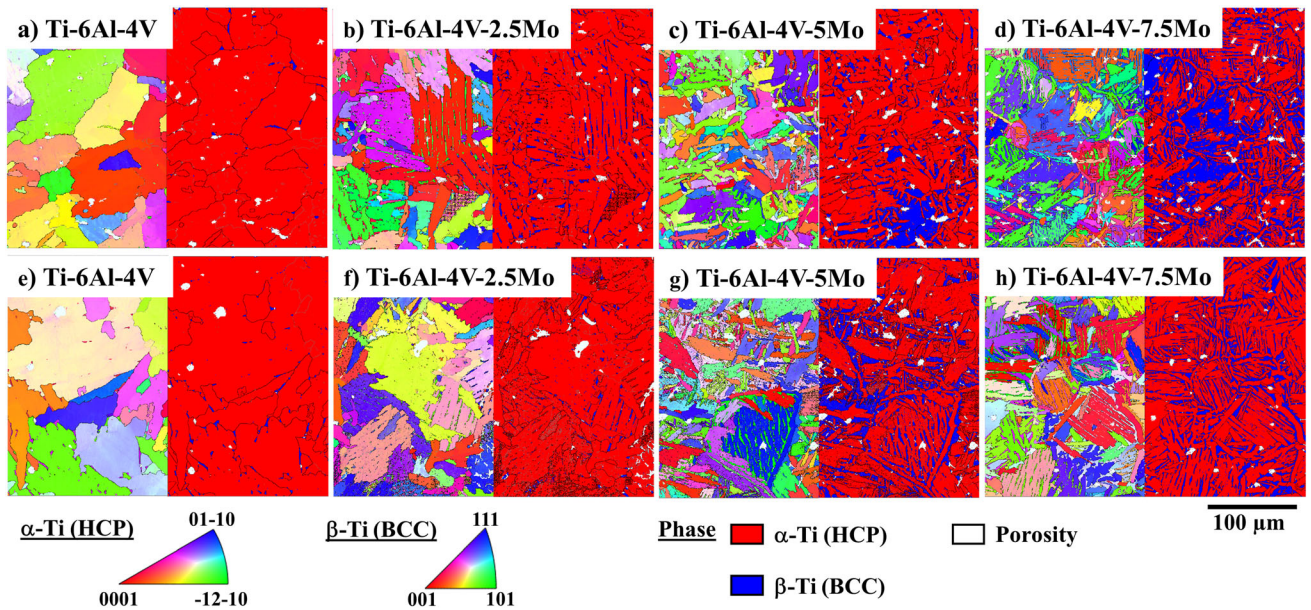


Fig. 9—Inverse pole figures (IPF) color and phase maps of Ti-6Al-4V-xMo alloys sintered at (a) to (d) 1100 and (e) to (h) 1150 °C for 4 h.

C. Fracture Surface Analysis

The fracture surfaces of Ti-6Al-4 V-xMo specimens, as shown in Figure 12, illustrate the mixture of ductile and brittle behaviors of all specimens evidenced by dimples and cleavage facets. The sintering temperature of 1150 °C results in a more brittle behavior for the Mo-free specimens compared to 1100 °C, which is consistent with a lower tensile strain to failure of the specimen sintered at 1150 °C. For the Mo-containing specimens, cracks are observed on the fracture surfaces, particularly in 5 and 7.5 wt pct Mo additions. The

high-magnification fractography at the crack region, along with the related EDS elemental mapping of Ti-6Al-4 V-7.5Mo specimen sintered at 1150 °C, as shown in Figure 13, confirms that the crack occurs at the TiC. The cross-sectional fracture surfaces (parallel to the tensile loading direction) of specimens are shown in Figure 14. The fracture area shows a transformation from transgranular fracture in low Mo contents to intergranular fracture in high Mo contents, with the evidence of cracks at TiC particles along the grain boundary, especially in the 5 wt pct Mo [Figures 6(c) and (g)] and 7.5 wt pct Mo [Figures 6(d) and (h)] alloys

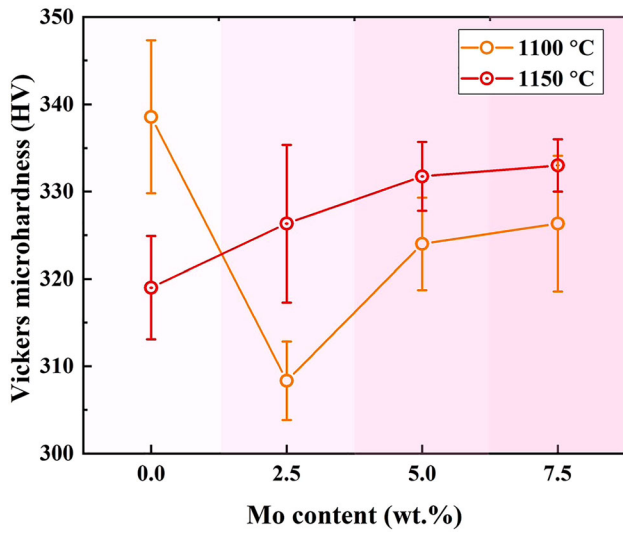


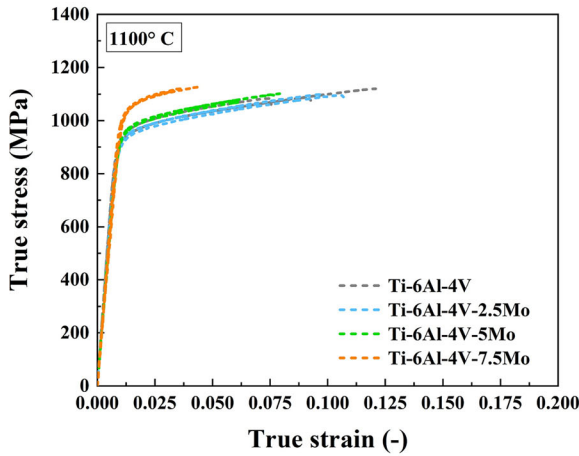
Fig. 10—Vickers microhardness of Ti-6Al-4V-xMo specimens sintered for 4 h.

for both sintering temperatures. Crack propagation along the porosity and α grain boundary in Mo-free specimens, and along the grain boundary, porosity, and TiC in Mo-containing specimens can be observed. These fracture characteristics are closely correlated with the tensile strain evolution, where the TiC formation results in lower tensile strain for the 5 and 7.5 wt pct Mo additions than the 2.5 wt pct Mo addition.

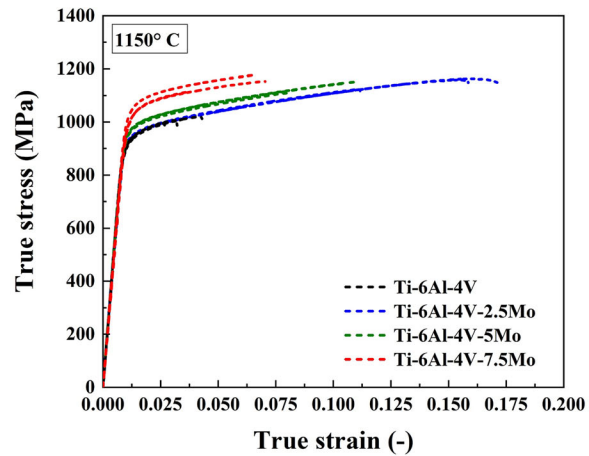
IV. DISCUSSIONS

A. Effect of Mo Content on Physical Properties and Microstructure

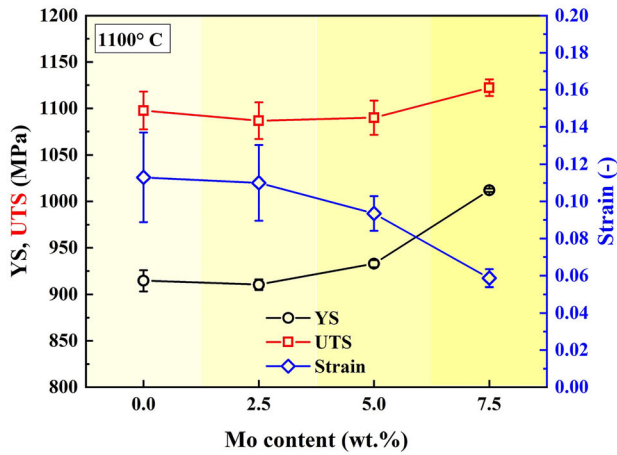
The additions of Mo in Ti-6Al-4 V result in decreasing relative sintered densities for both sintering temperatures. This decrease can be explained through the lower diffusivity of Mo compared to the self-diffusion of Ti, which is approximately one order of magnitude higher. The slower diffusion of Mo results in the formation of



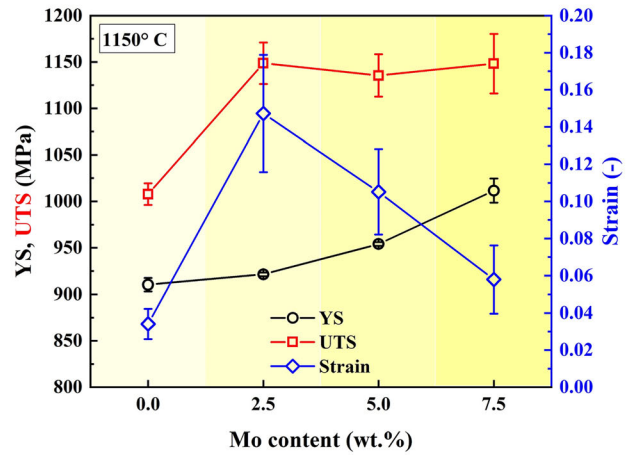
(a)



(b)



(c)



(d)

Fig. 11—Tensile properties: (a) to (b) true stress vs strain curves of Ti-6Al-4V-xMo alloys and (c) to (d) average true tensile properties of specimens.

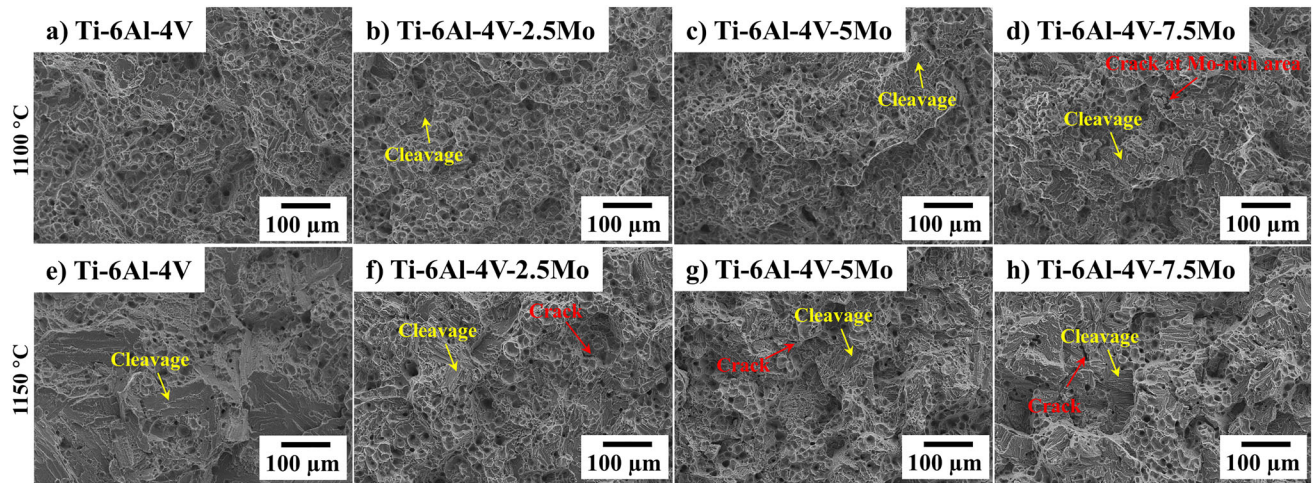


Fig. 12—Fractography (perpendicular to the loading direction) of Ti-6Al-4V-xMo alloys sintered at (a) to (d) 1100 and (e) to (h) 1150 °C for 4 h.

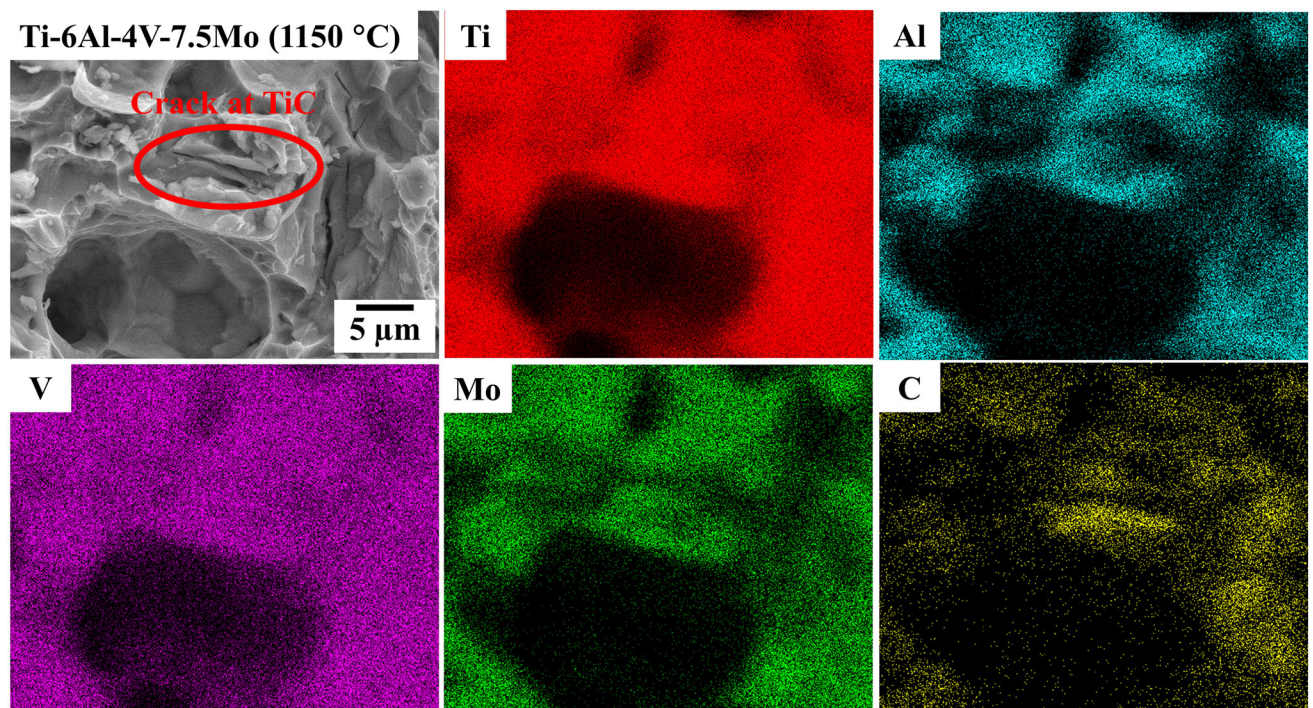


Fig. 13—Fractography of Ti-6Al-4V-7.5Mo specimen sintered at 1150 °C for 4 h with EDS elemental mapping, revealing a crack at the TiC.

more porosity. As a result, more remaining Mo-rich areas are observed as the Mo content increases, particularly when sintered at 1100 °C. The presence of these Mo-rich areas corresponds with Ti-Mo alloys sintered at insufficient sintering temperature,^[13] and they completely disappear when sufficient sintering temperature is used.

Mo has an important role in stabilizing β phase in Ti-6Al-4V, which is affected by the Mo content and cooling rate. The effects of different β stabilizers can be evaluated by considering the molybdenum equivalent, $[Mo_{eq}]$, which can be determined using Eq. [4] in wt pct^[45]:

$$[Mo_{eq}] = 1(\text{pct Mo}) + 0.67(\text{pctV}). \quad [4]$$

In the present study, the $[Mo_{eq}]$ was calculated by using the elemental contents from EDS analysis of all alloys, and the β phase fraction was determined through XRD analysis. The results are shown in Table IV. It is found that the $[Mo_{eq}]$ values for all alloys ranged from 1.9 to 9.1 wt pct, representing a typical $\alpha + \beta$ structure, which is in good agreement with the XRD and SEM results. Higher Mo contents lead to increase $[Mo_{eq}]$ values and consequently higher β phase fractions. Furthermore, the addition of 7.5 wt pct Mo promotes

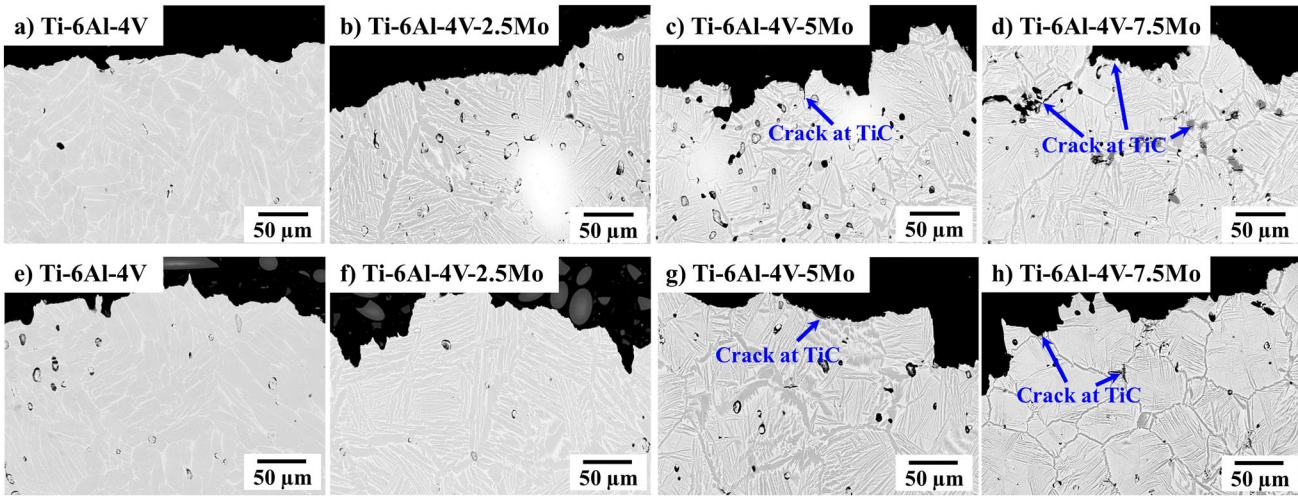


Fig. 14—Cross section (parallel to the loading direction) of Ti-6Al-4V-xMo alloys sintered at (a) to (d) 1100 and (e) to (h) 1150 °C for 4 h.

Table IV. Molybdenum Equivalent and β Phase Fraction of Alloys in the Present Study

Sintering Temperature	Alloys	[Mo _{eq}] (Wt Pct)	β Phase Fraction
1100 °C	Ti-6Al-4 V	1.9	9.7
	Ti-6Al-4 V-2.5Mo	4.4	20.6
	Ti-6Al-4 V-5Mo	6.6	39.9
	Ti-6Al-4 V-7.5Mo	9.1	45.4
1150 °C	Ti-6Al-4 V	1.9	17.1
	Ti-6Al-4 V-2.5Mo	4.3	20.6
	Ti-6Al-4 V-5Mo	7.0	36.1
	Ti-6Al-4 V-7.5Mo	9.0	48.0

the transformation of α to β phase and the formation of TiC, as the β phase has a lower C solubility limit than the α phase.^[37,38] The presence of this TiC is commonly observed in alloys with high β stabilizer contents fabricated by MIM, e.g., Ti-17Nb,^[46,47] Ti-20Nb-10Zr,^[16,17] Ti-(5-15)Mo,^[13] and fully β -structure Ti alloys, e.g., Ti-24Nb-4Zr-8Sn^[15] and Ti-27.5Nb-8.5Ta-3.5Mo-2.5Zr-5Sn.^[14]

B. Effect of Mo Content on Tensile Properties

Since all Ti-6Al-4 V-xMo alloys in this present study exhibit a dual $\alpha + \beta$ phase, the yield strength of the alloys can be explained through the rule of mixture^[48]:

$$\sigma_{YS} = f_a \sigma_a + f_b \sigma_b + \Delta\sigma_{iss} + \Delta\sigma_{Gb}, \quad [5]$$

$$\sigma_\alpha = \sigma_{\alpha \text{ matrix}} + \Delta\sigma_{d\alpha} + \Delta\sigma_{ss\alpha}, \quad [6]$$

$$\sigma_\beta = \sigma_{\beta \text{ matrix}} + \Delta\sigma_{d\beta} + \Delta\sigma_{ss\beta}, \quad [7]$$

where f_α and f_β are the volume fractions of the α and β phases. σ_α and σ_β are the yield strengths of the α and β phases. $\sigma_{\alpha \text{ matrix}}$ and $\sigma_{\beta \text{ matrix}}$ are critical slip-activation stresses of pure Ti for the α and β phases, which $\sigma_{\alpha \text{ matrix}} = 240 \text{ MPa}$ ^[49] and $\sigma_{\beta \text{ matrix}} = 219 \text{ MPa}$.^[50] $\Delta\sigma_{iss}$ is the interstitial solid-solution strengthening due to C,

N, and O as a function of O_{eq} content, which can be empirically interpolated following Reference 6, yielding a strengthening effect of 470.58 MPa/ wt pct of O_{eq} . $\Delta\sigma_d$, $\Delta\sigma_{ss}$, and $\Delta\sigma_{Gb}$ are the contributions of dislocation strengthening, solid-solution strengthening, and grain boundary strengthening.

The dislocation strengthening contribution can be calculated as follows:

$$\Delta\sigma_d = M\mu Gb\sqrt{\rho}, \quad [8]$$

where M is the Taylor factor, herein, for the α phase using 2.5 by assuming a prevalence of prism slip,^[49] and for the β phase using 2.8 by averaging the values of mixed (110, 112, 123) slip for bcc metal.^[51] μ represents the average strength of dislocation interaction, with a value of 0.3.^[51] G is the shear modulus (39 GPa). b is the burger vector, where $b = a$ for the hcp crystal (α phase) in the $\langle 11 \bar{2} 0 \rangle$ slip direction and $b = 0.866a$ for the bcc crystal (β phase) in the $\langle 111 \rangle$ slip direction. In addition, the lattice constants of all alloys utilized for calculation, obtained from the XRD analysis, are shown in Table V. ρ is the average dislocation density and described by an equation^[51]:

$$\rho = \frac{3E}{Gb^2(1+2\nu)} \epsilon_{micro}^2, \quad [9]$$

Table V. Parameters Associated with the Estimation of Yield Strength for All Alloys in this Work

Sintering Temperature (°C)	Alloys	Phase	Lattice Constant	Dislocation Density ($\times 10^{12}$)	Dislocation Strengthening (MPa)	Solid-Solution Strengthening (MPa)	Interstitial Strengthening (MPa)	Thickness of α Lamellae in Lamellar $\alpha + \beta$ Colonies (μm)	Grain boundary strengthening (MPa)	
1100	Ti-6Al-4 V	α	a = 2.9215 c = 4.6675	1.95	119.3	87.6	296.0	7.92 ± 3.32	34.1	
		β	a = 3.2130	3.98	181.9	300.2	341.7	3.79 ± 1.45	49.4	
	Ti-6Al-4 V-2.5Mo	α	a = 2.9208 c = 4.6682	1.03	86.7	96.8	260.4	1.30 \pm 0.63	84.1	
		β	a = 3.2262	3.64	174.7	332.1	266.3	0.53 ± 0.23	131.5	
	Ti-6Al-4 V-5Mo	α	a = 2.9112 c = 4.6612	1.18	92.6	100.7	305.0	7.96 ± 3.54	34.0	
		β	a = 3.2233	3.12	161.6	345.4	296.1	2.74 ± 1.12	58.0	
	Ti-6Al-4 V-7.5Mo	α	a = 2.9192 c = 4.6729	6.08	210.6	109.3	446.8	1.01 ± 0.61	95.3	
		β	a = 3.2298	11.64	312.6	374.9	436.0	0.47 ± 0.18	140.1	
	1150	Ti-6Al-4 V	α	a = 2.9144 c = 4.6682	1.73	112.1	88.6	305.0	7.96 ± 3.54	34.0
			β	a = 3.2120	4.14	185.5	303.8	296.1	2.74 ± 1.12	58.0
		Ti-6Al-4 V-2.5Mo	α	a = 2.9144 c = 4.6729	1.20	93.2	96.9	332.3	1.01 ± 0.61	95.3
			β	a = 3.2279	4.69	198.3	332.3	446.8	1.01 ± 0.61	95.3
Ti-6Al-4 V-5Mo		α	a = 2.9224 c = 4.6775	1.88	117.3	105.8	446.8	1.01 ± 0.61	95.3	
		β	a = 3.2315	3.90	181.0	362.8	436.0	0.47 ± 0.18	140.1	
Ti-6Al-4 V-7.5Mo		α	a = 2.9192 c = 4.6729	8.75	252.5	108.6	436.0	0.47 ± 0.18	140.1	
		β	a = 3.2298	14.71	351.4	372.4	436.0	0.47 ± 0.18	140.1	

where E and ν are the elastic modulus and Poisson's ratio, in which 102 GPa^[51] and 0.33 are used in this study, respectively. ε_{micro} is microstrain and can be obtained from XRD results.

The solid-solution strengthening contribution can be calculated using Eqs. [10] through [12] as suggested by Gypen and Toda-Caraballo^[51]:

$$\Delta\sigma_{ss} = \left(\sum_i B_i^{3/2} X_i \right)^{2/3}, \quad [10]$$

$$B_i = MG\lambda_i^{4/3}, \quad [11]$$

$$\lambda_i = \xi\phi(\eta_i, \delta_i), \quad [12]$$

where B_i is the coefficient of solid-solution strengthening. X_i is the content of solute i (at. pct), while Z is a temperature-dependent factor, which is 0.9×10^{-3} .^[52] λ_i is a misfit parameter responsible for the solute/solvent lattice parameter misfit (δ_i) and the shear modulus misfit (η_i) between Ti and foreign atoms.^[51,52] ξ is the factor that is responsible for the friction effect of slip system multiplicity and solute atoms.^[53] For bcc metals, ξ is 4.^[51] While for hcp metals with 12 potential slip systems, which are a quarter of bcc metals, ξ is 1. The B_i values are 285, 879, and 575 MPa/at^{2/3} for Al, V, and Mo in β phase, respectively^[51] and in α phase are 44.88, 138.43, and 90.56 MPa/at^{2/3}, respectively.

The grain boundary strengthening contribution can be expressed by the Hall–Petch equation^[54]:

$$\Delta\sigma_{Gb} = \sigma_0 + kD^{-1/2}, \quad [13]$$

where σ_0 and k are the intercept and the Hall–Petch slope, respectively. D is the average grain size, in which the average thickness of α lamellae in lamellar $\alpha + \beta$ colonies was proposed to use in the alloy with lamellar structure.^[55,56] This is because the α/β interface can impede dislocation movement, similar to the grain boundary in polycrystalline alloys. The thickness of α lamellae in lamellar $\alpha + \beta$ colonies, measured through image analysis (average from at least 3 images in each alloy), is shown in Table V. Figure 15 shows a strong correlation between the average thickness of α lamellae and the yield strength of all alloys, following the Hall–Petch relationship.

All parameters and calculated values following Eqs. [5] through [12] are reported in Table V. The overall strengthening contributions, as calculated using Eq. [5], are compared with the experimental values, as shown in Figure 16. It is found that the calculated values of overall strengthening exhibit a similar trend to the experimental values, in which yield strength increases with an increase in Mo contents for both sintering temperatures. According to the calculated values, the strengthening contributions of all alloys in the present study can be ranked from the highest to the lowest as follows: solid solution due to interstitial elements, solid solution by Al, V, and Mo and grain boundary strengthening. Nevertheless, there is a discrepancy

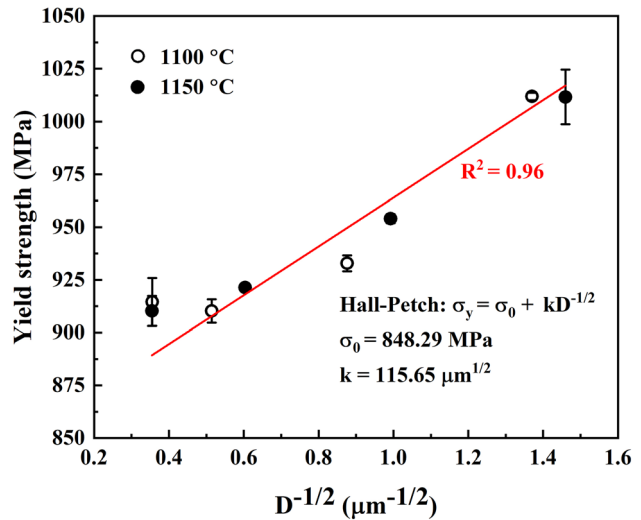


Fig. 15—Yield strength of all alloys sintered at 1100 and 1150 °C as a function of the average thickness of α lamellae in lamellar $\alpha + \beta$ colonies.

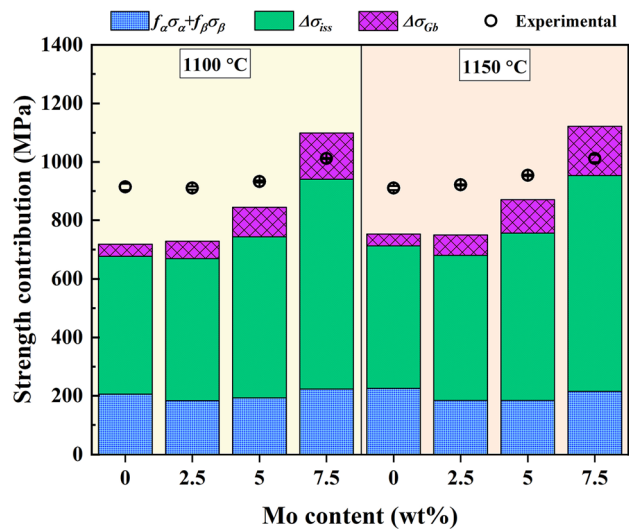


Fig. 16—Comparison between calculated strengthening contributions following Eq. [5] and experimental values for all alloys sintered at 1100 and 1150 °C.

between calculated and experimental values, which decreases with increasing Mo content. For Mo-free and Mo-containing alloys (2.5 and 5 wt pct Mo additions), this discrepancy can be attributed from two factors: (i) the effects of composition variations, especially impurities, which contribute significantly to the overall strengthening in the present study, and (ii) the presence of ultrafine α in β structure (indicated by green arrows in Figures 6 and 7), which potentially enhances the strength.^[43,44] These factors lead to lower calculated values compared to the experimental values. This discrepancy slightly decreases with 5 wt pct Mo addition, and the calculated values exceed the experimental values for both sintering temperatures in the case of 7.5 wt pct Mo addition. It can be explained by the reduction of solid-solution strengthening by Mo, resulting from an

insufficient sintering temperature to dissolve Mo as the Mo content increases. Furthermore, as reported in Reference 57, an excessively high fraction of Mo-rich area can also reduce the strength of Ti-Mo alloys produced by spark plasma sintering, using elemental CP-Ti and Mo powder.^[57]

Normally, the tensile strain in MIM $\alpha + \beta$ Ti alloys depends on three factors, which are relative sintered density, impurity, and TiC.^[6,13,37] In addition, as reported in Reference 22, the Ti-6Al-4 V-(2, 4)Fe strain also depends on the volume fraction of grain boundary α layers. Considering the relative sintered density, all alloys in the present study exhibit similar values, resulting in a negligible effect on the strain to failure. Regarding the effect of impurity contents, the impurity contents have a strong impact on the Mo-free specimens. The higher sintering temperature leads to a higher oxygen content due to increased oxidation at the elevated temperature. Consequently, this decreases the strain to failure of Ti-6Al-4 V alloys sintered at 1150 °C compared to those sintered at 1100 °C.

However, in Mo-containing specimens, the impurity is not the primary factor influencing the strain to failure. It can be observed that a higher sintering temperature does not result in a reduction in strain to failure. Considering the alloy with 2.5 wt pct Mo addition sintered at 1150 °C, the strain is significantly higher compared to 1100 °C. This is due to the increased dissolution of Mo at the higher sintering temperature, leading to the formation of a fine α and β structure without the evidence of brittle TiC. Consequently, there is a higher volume fraction of grain boundary α layers, which contributes to an increase in strain. However, for alloys with 5 and 7.5 wt pct Mo additions, although there is a higher fraction of grain boundary α layers due to the Mo additions, the formation of brittle TiC becomes more prominent. The negative effect of TiC outweighs the positive effect of higher grain boundary α layers, resulting in a lower strain to failure. This is confirmed by the cross-sectional fracture surfaces (Figure 14), where the presence of TiC can be observed in the fracture area. Based on this study, it can be concluded that 5 wt pct Mo addition is considered the threshold for the detrimental effects of TiC on strain to failure.

V. CONCLUSIONS

Herein, the influences of Mo additions (2.5, 5, and 7.5 wt pct) to Ti-6Al-4 V alloys fabricated by MIM at 1100 and 1150 °C sintering temperatures were investigated. The following conclusions can be summarized:

1. Ti-6Al-4 V alloys with and without Mo additions can be fabricated by the MIM process, achieving the relative sintered density of over 98.25 pct for Mo-free specimens and over 96.75 pct for Mo-containing specimens.
2. The microstructure of the alloys undergoes a transformation from α and β lamella or partly lamella in Mo-free specimens to a fine lamella

structure in Mo-containing specimens. The fraction of β phase increases with increasing Mo contents and the lamellar becomes finer. In addition, the presence of TiC is observed in alloys with 5 and 7.5 wt pct Mo additions.

3. The mechanical properties are strongly influenced by the sintering temperatures and Mo contents. For Mo-free alloys, the 1100 °C sintering temperature results in higher tensile strain than 1150 °C due to the effect of impurity content. However, the 1100 °C sintering temperature is not sufficient to effectively dissolve Mo into the Ti-6Al-4 V alloy, leading to lower tensile properties than 1150 °C. The alloy with 2.5 wt pct Mo addition, sintered at 1150 °C, provides the optimum balance between tensile strength (921 MPa) and strain to failure (15 pct) in this study. Exceeding 2.5 wt pct Mo addition, the strain begins to decrease, with 5 wt pct Mo addition considered as the threshold.
4. The strengthening contribution of alloys can be explained through solid-solution strengthening, interstitial strengthening, and grain boundary strengthening by α lamellae. The strain to failure improves with a higher volume fraction of grain boundary α layers induced by Mo content. However, at higher Mo contents (5 and 7.5 wt pct Mo), the fracture is dominated by TiC, which can be potential crack initiation sites, leading to lower tensile strain.

ACKNOWLEDGMENTS

This work has received financial support from National Metal and Materials Technology Center (MTEC) and Taisei Kogyo (Thailand) Co., Ltd. (Grant No. P2150585). The authors would also like to express their gratitude to Prof. Katsuyoshi Kondoh from Osaka University, Japan for his assistance with the impurity measurements. In addition, the authors would like to thank Mr. Prathomoom Newyawong and Mr. Natapong Wongpanya from the Microscopy Laboratory, NSTDA Characterization and Testing Service Center, National Sciences and Technology Development Agency (NSTDA), Thailand for their support.

AUTHOR CONTRIBUTIONS

CS: conceptualization, methodology, investigation, visualization, writing original draft, writing—review and editing. SS: methodology and investigation. MT: conceptualization, methodology, and resources. AM: conceptualization, resources, writing—review and editing, supervision, project administration, and funding acquisition.

CONFLICTS OF INTEREST

The authors declare that they have no known competing financial interests or personal relationships that could have appeared to influence the work reported in this paper.

DECLARATION OF GENERATIVE AI IN SCIENTIFIC WRITING

During the preparation of this work, the author(s) used ChatGPT / Open AI in order to proofread this manuscript. After using this tool/service, the authors reviewed and edited the content as needed and take full responsibility for the content of the publication.

REFERENCES

1. I. Polmear: *Light Alloys: From Traditional Alloys to Nanocrystals*, Elsevier, Amsterdam, 2005.
2. S.Y. Hong, I. Markus, and W.-C. Jeong: *Int. J. Mach. Tools Manuf.*, 2001, vol. 41, pp. 2245–60.
3. K. Kudo, K. Shinagawa and H. Miura: *Mech. Eng. J.* 2018, vol. 5, pp. 17-00686-17-86.
4. F.H. Froes, S.J. Mashl, J.C. Hebeisen, V.S. Moxson, and V.A. Duz: *JOM*, 2004, vol. 56, pp. 46–48.
5. C. Suwanpreecha and A. Manonukul: *SIAM Sci. Innov. Adv. Mater.*, 2021, vol. 1, pp. 64005–64105.
6. T. Ebel: In *Handbook of Metal Injection Molding*, ed. D. F. Heaney Woodhead Publishing: 2012, pp 415-45.
7. S. Bootchai, N. Taweejun, A. Manonukul, and C. Kanchanomai: *J. Mater. Eng. Perform.*, 2020, vol. 29, pp. 1–10.
8. A.T. Sidambe, I.A. Figueroa, H.G.C. Hamilton, and I. Todd: *J. Mater. Process. Technol.*, 2012, vol. 212, pp. 1591–97.
9. A.A. Hidalgo, T. Ebel, W. Limberg, and F. Pyczak: *Key Eng. Mater.*, 2016, vol. 704, pp. 44–52.
10. G.C. Obasi, O.M. Ferri, T. Ebel, and R. Bormann: *Mater. Sci. Eng. A*, 2010, vol. 527, pp. 3929–35.
11. O.M. Ferri, T. Ebel, and R. Bormann: *Mater. Sci. Eng. A*, 2010, vol. 527, pp. 1800–05.
12. O.M. Ferri, T. Ebel, and R. Bormann: *Mater. Sci. Eng. A*, 2009, vol. 504, pp. 107–13.
13. C. Suwanpreecha, S. Songkuea, P. Wangjina, M. Tange, W. Pongsaksawad and A. Manonukul: *Met. Mater. Int.*, 2023.
14. C. Suwanpreecha, E. Alabort, Y.T. Tang, C. Panwisawas, R.C. Reed, and A. Manonukul: *Mater. Sci. Eng. A*, 2021, vol. 812, p. 141081.
15. F. Kafkas and T. Ebel: *J. Alloys Compd.*, 2014, vol. 617, pp. 359–66.
16. P. Xu, F. Pyczak, W. Limberg, R. Willumeit-Römer, and T. Ebel: *Mater. Des.*, 2021, vol. 211, p. 110141.
17. P. Xu, F. Pyczak, M. Yan, W. Limberg, R. Willumeit-Römer, and T. Ebel: *Appl. Mater. Today*, 2020, vol. 19, p. 100630.
18. W. Limberg, T. Ebel, F. Pyczak, M. Oehring, and F.P. Schimansky: *Mater. Sci. Eng. A*, 2012, vol. 552, pp. 323–29.
19. Y. Liu, Y. Pan, X. Lu, J. Sun, T. Hui, Y. Yang, A. Yu, X. Qu, and J. Zhang: *Powder Technol.*, 2021, vol. 384, pp. 132–40.
20. D. Banerjee and J.C. Williams: *Acta Mater.*, 2013, vol. 61, pp. 844–79.
21. W. Weng, A. Biesiekierski, Y. Li, and C. Wen: *Materialia*, 2019, vol. 6, p. 100323.
22. L. Meng, Y. Zhang, X. Zhao, and D. Zhang: *Mater. Sci. Eng. A*, 2021, vol. 825, p. 141877.
23. Y. Itoh, H. Miura, T. Uematsu, T. Osada, and K. Sato: *J. Solid Mech. Mater. Eng.*, 2009, vol. 3, pp. 921–30.
24. P. Zhao, Y. Song, K. Dong, D. Shan, and E.-H. Han: *J. Alloys Compd.*, 2021, vol. 858, p. 157708.
25. P.L. Narayana, S. Lee, S.-W. Choi, C.-L. Li, C.H. Park, J.-T. Yeom, N.S. Reddy, and J.-K. Hong: *J. Alloys Compd.*, 2019, vol. 811, p. 152021.
26. G. Chen, Q. Zhai, Z. Ma, X. Yin, Q. Zhang, H. Zhou, L. Meng, K. Wang, S. Wang, and L. Wang: *Mater. Technol.*, 2022, vol. 37, pp. 1062–1074.
27. D. Wu, W.-L. Wang, L.-G. Zhang, Z.-Y. Wang, K.-C. Zhou, and L.-B. Liu: *Int. J. Miner. Metall. Mater.*, 2019, vol. 26, pp. 1151–65.
28. Y. Itoh, T. Uematsu, K. Sato, H. Miura, and M. Niinomi: *J. Jpn. Soc. Powder Powder Metall.*, 2006, vol. 53, pp. 750–54.
29. R. Yamanoglu, A. Bahador, and K. Kondoh: *J. Mater. Eng. Perform.*, 2021, vol. 30, pp. 3203–12.
30. M. Rajadurai, A. Muthuchamy, A.R. Annamalai, D.K. Agrawal, and C.-P. Jen: *Molecules*, 2021, vol. 26, p. 2894.
31. C. Sun, R. Xiao, H. Li, and Y. Ruan: *Corros. Sci.*, 2022, vol. 200, p. 110232.
32. B.-S. Sung, T.-E. Park and Y.-H. Yun: *Adv. Mater. Sci. Eng.*, 2015, vol. 2015.
33. D. Mareci, R. Chelariu, D. Gordin, M. Romas, D. Sutiman, and T. Gloriant: *Mater. Corros.*, 2010, vol. 61, pp. 829–37.
34. D. Mareci, R. Chelariu, I. Dan, D.-M. Gordin, and T. Gloriant: *J. Mater. Sci. Mater. Med.*, 2010, vol. 21, pp. 2907–13.
35. W. Xu, X. Lu, L.N. Wang, Z.M. Shi, S.M. Lv, M. Qian, and X.H. Qu: *J. Mech. Behav. Biomed. Mater.*, 2018, vol. 88, pp. 534–47.
36. J. Takekawa and N. Sakurai: *J. Jpn. Soc. Powder Powder Metall.*, 1999, vol. 46, pp. 877–81.
37. D.-P. Zhao, T. Ebel, M. Yan, and M. Qian: *JOM*, 2015, vol. 67, pp. 2236–43.
38. M. Yan, M. Qian, C. Kong, and M.S. Dargusch: *Acta Biomater.*, 2014, vol. 10, pp. 1014–23.
39. X. Luo, T. Ebel, F. Pyczak, W. Limberg, and Y. Lin: *Mater. Lett.*, 2017, vol. 193, pp. 295–98.
40. Y. Liu, W.-F. Wei, K.-C. Zhou, L.-F. Chen, and H.-P. Tang: *J. Cent. South Univ.*, 2003, vol. 10, pp. 81–86.
41. S. Özbilen, D. Liebert, T. Beck, and M. Bram: *Mater. Sci. Eng. C*, 2016, vol. 60, pp. 446–57.
42. É. Baril: *Powder Inject. Mould. Int.*, 2010, vol. 4, pp. 22–32.
43. M. Yan, M. Dargusch, T. Ebel, and M. Qian: *Acta Mater.*, 2014, vol. 68, pp. 196–206.
44. A. A. Hidalgo, T. Ebel, R. Frykholm, E. Carreño-Morelli and F. Pyczak: *Mater. Today Commun.*, 2022, p. 104982.
45. G. Welsch, R. Boyer, and E. Collings: *Materials Properties Handbook: Titanium Alloys*, ASM International, Washington, DC, 1993.
46. J. Bidaux, C. Closuit, M. Rodriguez-Arbaizar, D. Zufferey, and E. Carreño-Morelli: *PIM Int.*, 2012, vol. 6, pp. 72–75.
47. J.-E. Bidaux, R. Pasquier, M. Rodriguez-Arbaizar, H. Girard, and E. Carreño-Morelli: *Powder Metall.*, 2014, vol. 57, pp. 320–23.
48. Y. Fu, W. Xiao, J. Wang, L. Ren, X. Zhao, and C. Ma: *J. Mater. Sci. Technol.*, 2021, vol. 76, pp. 122–28.
49. Y. Zhang, S. Fang, Y. Wang, and D. Zhang: *Mater. Sci. Eng. A*, 2021, vol. 803, p. 140701.
50. S. Huang, Y. Zhao, J. Yu, C. Lin, C. Wu, and W. Jia: *J. Alloys Compd.*, 2020, vol. 826, p. 154128.
51. G.H. Zhao, X.Z. Liang, B. Kim, and P.E.J. Rivera-Díaz-del-Castillo: *Mater. Sci. Eng. A*, 2019, vol. 756, pp. 156–60.
52. A. Bahador, J. Umeda, R. Yamanoglu, T.A. Abu Bakar, and K. Kondoh: *Mater. Sci. Eng. A*, 2021, vol. 800, p. 140324.
53. I. Toda-Caraballo and P.E. Rivera-Díaz-del-Castillo: *Acta Mater.*, 2015, vol. 85, pp. 14–23.
54. N. Hansen: *Scr. Mater.*, 2004, vol. 51, pp. 801–06.
55. M. Jia, D. Zhang, J. Liang, and B. Gabbitas: *Metall. Mater. Trans. A*, 2017, vol. 48, pp. 2015–29.
56. S. Semiati and T. Bieler: *Acta Mater.*, 2001, vol. 49, pp. 3565–73.
57. M. Shahedi Asl, S.A. Delbari, M. Azadbeh, A. Sabahi Namini, M. Mehrabian, V.-H. Nguyen, Q.V. Le, M. Shokouhimehr, and M. Mohammadi: *J. Mater. Res. Technol.*, 2020, vol. 9, pp. 10647–58.

Publisher's Note Springer Nature remains neutral with regard to jurisdictional claims in published maps and institutional affiliations.

Springer Nature or its licensor (e.g. a society or other partner) holds exclusive rights to this article under a publishing agreement with the author(s) or other rightsholder(s); author self-archiving of the accepted manuscript version of this article is solely governed by the terms of such publishing agreement and applicable law.